EurJIC
European Journal of Inorganic Chemistry

Research Article
doi.org/10.1002/ejic.202400769

Chemistry Europe
European Chemical Societies Publishing

www.eurjic.org

Instigating Visible Light Inspired DNA Impairment by ROS Harvesting Ir(III)-Cyclometallated Imidazophenanthroline Complexes Against MDA-MB-231 Cells

Sreejani Ghosh[a] and Priyankar Paira*[b]

Difficulties to abate the vehemence of deleterious triple-negative breast cancer (TNBC) is an ardent issue in the current context of anticancer research due to the lack of a selective treatment modality. To address this issue, herein we have endeavored to establish the imidazophenanthroline-based Ir-(III)-cyclometallated heteroleptic complexes, suited for the one-photon photodynamic therapy (OP-PDT) under irradiation of visible light (400–700 nm) possessing long-lived excited triplet state and significant photostability. Among three synthesized complexes, [**L1Ir**], [**L2Ir**], [**L3Ir**], the complex [**L2Ir**] has been recognized as the most competent complex to exhibit selective phototoxicity ($IC_{50} = 3.8\ \mu M$; $PI^c = 78.94$) in MDA-MB-231 triple-negative breast cancer cells. The significant phototoxicity of the complexes has arisen due to the production of reactive singlet oxygen ($^1O_2$) following the type-II pathway ($\Phi_s = 0.26$). Also, the complexes have shown the proficiency in oxidation of reduced nicotinamide adenine dinucleotide (NADH) ($TOF = 37.82\ h^{-1}$) indicating the possibility of reactive oxygen species ($O_2^{\bullet-}$, $^{\bullet}OH$) generation through type-I pathway upon visible light irradiation. Along with this, intracellular glutathione (GSH) depletion capabilities have endued the complexes to unarm the TNBC cells in front of the profuse amount of ROS instigating the programmed cell death (PCD) through substantial DNA damage.

1. Introduction

Cancer renders as one of the most severe and perilous ailments affecting people throughout the world.[1] The avoidance of apoptosis, uncontrolled proliferation, hindrance to anti-growth signals and provocation of own growth signals, amplified angiogenesis as well as unbridled metastasis of tumour tissues can be considered as the primary causes of mortality due to cancer.[2] In 2024, the National Cancer Institute (NCI) unveiled a statistical report of 2,001,140 new cases of cancer in the United States and the number of deaths is 611,720. As a second leading cause of death, it is expected that the death toll for cancer will be more than 13.1 million by 2030.[3] Among various types of cancer, breast cancer (BC) has been diagnosed as the most prevailing malignancy of women worldwide and has secured the second place in the list of cancer-related mortality as per the satistical report of the World Health Organization (WHO) and Global Cancer Statistics of GLOBOCAN.[4] BC is broadly categorized as human epidermal growth factor receptor 2 (HER-2) enriched, hormone receptor (HR) positive, and triple-negative based on the expression of biomarkers, viz Ki67, human epidermal growth factor receptor 2 (HER2), estrogen receptors (ER), and progesterone receptors (PR). Triple-negative breast cancer (TNBC) is deprived of the hormone receptors as well as the human epidermal growth factor receptors 2 (HER2) and has been identified as the most hostile and heterogeneous subtypes with poor prognosis among all types of breast cancer.[5] The gene expression profile of TNBC characterizes this cancer as basal-like breast cancer (BLBC), which occurs due to mutation in BRCA1/2 gene patterns.[6] Chemotherapy is generally employed to cure the basal type of breast cancer, but different gene patterns of the TNBC subtypes necessitate a particular therapeutic approach instead of a generalized one.[7] Therefore in the current phase of anticancer research, there are different therapeutic approaches for treating normal breast cancer, but there is no proper treatment regimen to subdue the unbridled triple-negative breast cancer.[8] Although the stupendous discovery of cisplatin by Rosenberg in the 1960s paved the way for metal complexes in cancer therapy, the usage of platinum complexes in chemotherapy was restricted owing to their unavoidable side effects including drug resistance, neurotoxicity, nephrotoxicity, hepatotoxicity, and treatment selectivity.[9] Unfortunately, shortcomings associated with chemotherapy, radiation therapy, and surgery along with drug resistance, have made the treatment of cancers very challenging. In recent times, photodynamic therapy (PDT) has garnered profound interest as a potentially superior cancer healing strategy.[10] Importantly, PDT unveils numerous benefits over conventional treatment modalities such as surgery or chemotherapy. The lower invasiveness, great selectivity, and incredible efficiency, along with less detrimental side effects, have established this therapy as the most significant current strategy for treating cancer.[11] This method leverages light and photosensitizers (PSs) to transform molecular oxygen into reactive oxygen species (ROS), which can adeptly assassinate the

[a] S. Ghosh
Department of Chemistry, School of Advanced Sciences (SAS), Vellore Institute of Technology (VIT), Vellore – 632014, Tamil Nadu, India

[b] P. Paira
Department of Chemistry, School of Advanced Sciences (SAS), Vellore Institute of Technology (VIT), Vellore – 632014, Tamil Nadu, India
E-mail: priyankar.paira@vit.ac.in

Supporting information for this article is available on the WWW under https://doi.org/10.1002/ejic.202400769

Research Article
doi.org/10.1002/ejic.202400769

affected tissues in the body.[12] On the other hand, the generation of ROS is closely linked to the non-radiative intersystem crossing (ISC) from excited singlet states (S_n) to excited triplet states (T_1). PSs are activated and then change their states when they are exposed to light: they first move from the ground state (S_0) to the different excited singlet states (S_n) and then they change the spin state undergoing non-radiative intersystem crossing (ISC) to move to the excited T_1 state depending on the energy gaps (ΔE_{ST}) between the singlet (S_1) and triplet (T_1) excited states. Therefore, this movement may either result in fluorescence induced by a radiation pathway or a radiative phosphorescence pathway from the T_1 to S_0 state. Cancer cells are eliminated by the photosensitizer's excited triplet state, which changes the ground state $^3O_2$ into active singlet oxygen ($^1O_2$). This step has been designated as a type II reaction. Electron transfer mechanisms, also known as type I reactions, are accountable for the generation of radical species, namely superoxide ion ($O_2^{\bullet-}$) and hydroxyl radical ($^{\bullet}OH$).[13] The remarkable attributes of Ir(III) organometallic compounds enabled researchers to formulate various kinds of cationic cyclometalated Ir(III)-based metal complexes that are excellent cellular imaging agents. The following are the reasons for their use in imaging: (i) large Stokes shifts (> 100 nm) for minimizing inner filter effects; (ii) rapid transmembrane activity (short incubation time and less potential toxicity); (iii) long luminescence lifetimes (100 ns) for time-resolved detection; and (iv) enhanced photostabilities (less photobleaching).[14] Additionally, several kinds of Ir(III) complexes have been investigated recently as anticancer theranostic drugs; and Ir(III) cyclometalated complexes have come to lime-light as powerful photodynamic therapeutic agents.[15] These complexes demonstrated the ability to identify the cancer cells in the human body and then their destruction either by disrupting DNA or by triggering the mitochondrial malfunction via the release of reactive oxygen species (ROS).[16] Furthermore, given their high-lying metal-centered states and flexibly modifiable highest occupied molecular orbital (HOMO) and lowest unoccupied molecular orbital (LUMO) energy levels, heteroleptic Ir(III) complexes with bidentate (NN) ligands and cyclometallation with (CN) ligands have demonstrated excellent photostability.[17] Cyclometalated Ir(III) complexes, exhibiting a high photostability, render them useful for continuous irradiation and real-time intracellular transport and accumulation monitoring.[18] The aforementioned complexes can also disturb the cell cycle by oxidizing NADH and demolishing the energy currency in cancer cells. Also, glutathione (GSH), an important antioxidant elevated in cancer cells, can be depleted by cyclometalated iridium (III) complexes, propelling the cells more towards oxidative stress, which promotes substantial programmed cell death (Figure 1).[19]

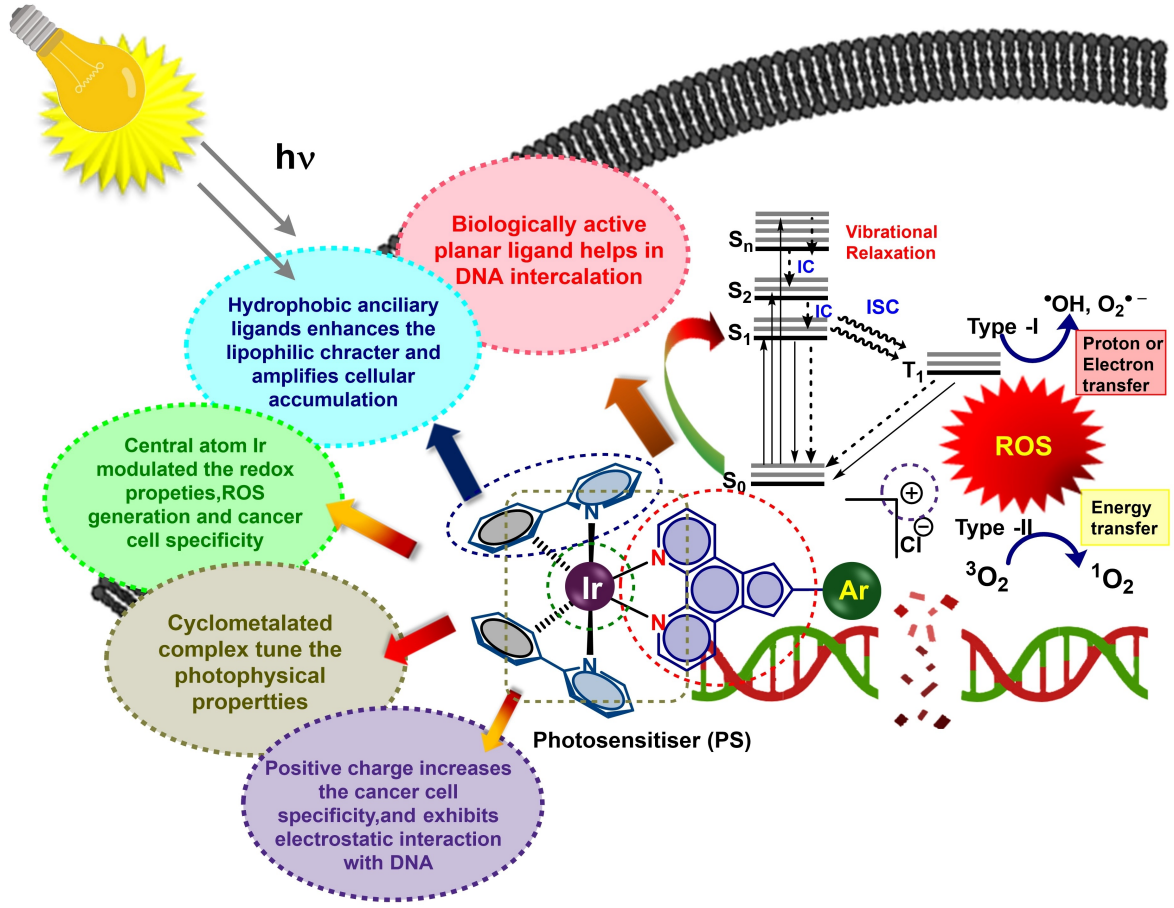

Figure 1. Design of the cyclometallated complexes.

Research Article
doi.org/10.1002/ejic.202400769

2. Results and Discussion

2.1. Synthesis and Characterization

The process described in Scheme 1 was followed to synthesize the ligands **L1**–**L3** as well as their corresponding complexes, [**L1Ir**], [**L2Ir**], [**L3Ir**]. To synthesize the ligands (**L1**–**L3**), we followed our previously established protocol.[20] After 30 h of reflux reaction involving [1,10]-phenanthroline-5, 6-dione and three respective aryl aldehydes (naphthaldehyde, anthranaldehyde, and chromone aldehyde) in 1 : 1 molar ratio by dissolving the reacting components in minimum volume of glacial acetic acid with excess ammonium acetate, we were able to detect the formation of desired ligands (**L1**–**L3**) by monitoring the progression of the reaction through thin layer chromatography (TLC). Then the product was precipitated out upon neutralization by ice-cold ammonium hydroxide solution and we obtained the crude product after filtration. The crude product was washed thoroughly with hexane and diethyl ether to remove the impurities and a recrystallization technique was used to obtain the pure crystalline products. The structural confirmation of the ligands was obtained by ^{1}H and ^{13}C nuclear magnetic resonance (NMR) spectroscopy, Fourier transform infrared (FT-IR) spectroscopy, high-resolution mass spectrometry (HRMS), and purity of the ligands were analyzed by C, H, N analytical technique, which have been already reported from our group. Bright yellow-coloured iridium precursor ([**IrCP**]) was taken in a pear-shaped flask and it was dissolved properly in 10 ml of 4: 1 toluene/methanol solvent mixture to get a clear yellowish solution. Then 2.1 equivalents of the previously prepared pure ligand (**L1**/**L2**/**L3**) were added to the solution of iridium precursor ([**IrCP**]) and sonicated for 5 minutes to get a clear brownish-coloured solution upon thoroughly mixing the reactants. Thereafter, the reaction mixture was refluxed for 6 h in N_2-atmosphere at 120 °C. The progression of the reaction was periodically monitored by thin-layer chromatography (TLC) using 100% methanol as a solvent system. At around 6 h of reflux, we observed a significant change in the colour of the reaction mixture from pale brown to dark brown, and the completion of the reaction was confirmed by re-performing the TLC. After cooling the reaction mixture at room temperature, the product was seen to be precipitated out. Then, we obtained the crude product after filtration. The crude product was repeatedly washed with hexane as well as hexane-ethyl acetate

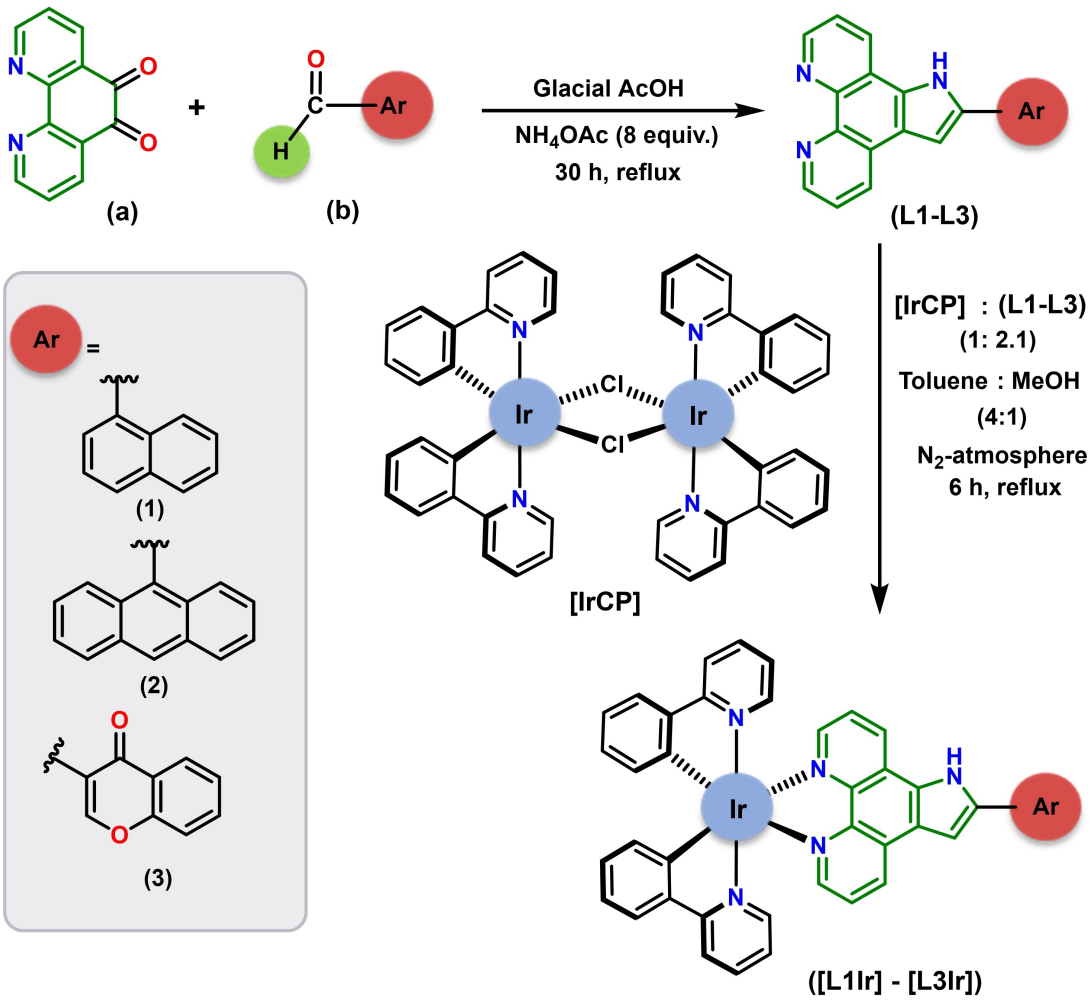

Scheme 1. Synthetic route for the formation of [**L1Ir**], [**L2Ir**] and [**L3Ir**] complexes.

Research Article
doi.org/10.1002/ejic.202400769

mixture (3:1) 5–6 times to remove impurities and the purity of the product was checked by performing the TLC. The cleaned product was then dried and subjected to recrystallization from methanol/diethyl ether to obtain more purified product. The crystalline product of each complex was weighed in a weighing balance and the % yield was calculated. In due course, the complexes [**L1Ir**], [**L2Ir**], and [**L3Ir**] were obtained as deep yellow to reddish brown coloured crystals with high yields (94–96%). The structures of all the complexes were assured by ^{1}H, ^{13}C NMR, FT-IR spectroscopy, and HRMS. The purity of the complexes was scrutinized by ultraperformance liquid chromatography (UPLC) as well as with C, H, N analysis.

2.1.1. Photophysical Characterization

Susceptibility towards the light is an important asset for designing a phototherapeutic anticancer drug. To ratify the photosensitizing ability of the synthesized complexes, namely [**L1Ir**], [**L2Ir**], and [**L3Ir**], we precisely evaluated their absorption and emission characteristics in a de-aerated acetonitrile medium at a constant pH of 7.4 and a temperature of 25 °C.

2.1.1.1. UV-Visible Spectra

In the absorption spectra, a similar type of absorption band with five different regions has been identified for each of the three complexes with different intensities (Figure 2a). These absorption bands can be broadly categorized as $\pi\rightarrow\pi^*$, LMCT, and MLCT. The more intense higher energy absorption bands at lower wavelength UV region (240–312 nm) had arisen due to the spin-allowed ligand-centered (^{1}LC) $\pi\rightarrow\pi^*$ transition (^{1}LLCT/^{1}ILCT), then lower energy comparatively less intense absorption bands at next higher wavelength region λ_{abs}: 312–358 nm, was observed because of spin-allowed ligand-centered (^{1}LC) ligand to metal charge transfer (^{1}LMCT) transitions. The least intense lower energy absorption bands at higher wavelength visible region (358–515 nm) were envisioned for spin-allowed metal-centered (^{1}MC) metal-to-ligand charge transfer (^{1}MLCT) transitions. In the ligand-centered (^{1}LC) electronic transition, the first absorption bands at shorter wavelength region, λ_{abs}: 240–282 nm ([**L2Ir**]$_{\lambda max}$ = 253 nm; [**L1Ir**]$_{\lambda max}$ = 260 nm and [**L1Ir**]$_{\lambda max}$ = 273 nm) was designated as spin-allowed charge transfer transition from filled π-MOs of 2-phenyl pyridine C^N ligand to vacant π*-MOs of imidazophenanthroline N^N ligand (^{1}LLCT: $\pi_{ppy}\rightarrow\pi_{imidazophen}$*); the second absorption band in ^{1}LC transition at next shorter wavelength region, λ_{abs}: 282–312 nm (λ_{max}~295 nm) was due to spin-allowed charge transfer transition from filled π-MOs to vacant π*-MOs of imidazophenanthroline N^N ligand (^{1}ILCT: $\pi_{imidazophen}\rightarrow\pi_{imidazophen}$*). The absorption band at λ_{abs}: 312–358 nm (λ_{max}~332 nm) appeared due to spin-allowed electronic transition from filled π-MOs of π-donor 2-phenyl pyridine C^N ligand to metal vacant dπ (t_{2g}/e_g) MOs [^{1}LMCT: π(C^N)→dπ(Ir)]. In the MLCT region (λ_{abs}: 358–515 nm), the first low intensity most important weak absorption bands for all the complexes were due to spin-allowed metal to ligand charge transfer transition (^{1}MLCT), observed at λ_{abs}: 358–425 nm (λ_{max}~390 nm) indicating the charge transfer transition from filled dπ (t_{2g}) MOs of metal to high energy vacant π*-MOs of imidazophenanthroline N^N ligand [^{1}MLCT: dπ(Ir)→π* (N^N)]. The insignificant low-intensity weakest absorption tails at higher wavelength region λ_{abs}: 425–515 nm (Figure 2a inset) might be indicated as the admixture of spin-forbidden ^{3}MLCT and ^{3}ILCT/^{3}LLCT transitions as a result of spin-orbit coupling (SOC) allowing intersystem crossing (ISC) from singlet excited to triplet excited states, which was essential for enabling PDT (Figure 2a). The theoretical investigation of electronic transitions for complex, [**L2Ir**] from highest occupied molecular orbital (HOMO) to lowest unoccupied molecular orbital (LUMO) also supported the significant metal-to-ligand charge transfer transition as an exclusive phenomenon for these complexes (Figure 2b). All the plausible electronic transitions associated with these complexes have been picturized schematically in Figure 2c.

2.1.1.2. Emission Spectra

Emission spectral analysis of these cyclometallated complexes was very crucial to get a clear vision of the probable pathways of ROS formation during PDT and hence we investigated the emission properties of each complex in de-aerated acetonitrile by exciting the molecules at respective ^{1}MLCT regions ([**L1Ir**]λ_{ex} = 390 nm, [**L2Ir**]λ_{ex} = 382 nm, [**L3Ir**]λ_{ex} = 395 nm). It was observed that complexes, [**L1Ir**] and [**L3Ir**] displayed a single intense emission band at λ_{em} = 572 nm with very large Stokes' shift of 180 nm and 177 nm, respectively indicating the possibility of phosphorescence as an emission phenomenon from the lowest-lying triplet excited state to singlet ground state (Figure 2e). On the other hand, complex, [**L2Ir**] unveiled dual emission representing two emission bands: one is at a higher energy region (λ_{em} = 438 nm) with Stokes' shift of 56 nm and another is at a lower energy region (λ_{em} = 572) with Stokes' shift of 190 nm, which attributed the complex, [**L2Ir**] a special characteristic for exhibiting both fluorescence and phosphorescence phenomena simultaneously (Figure 2e). The emission at 438 nm with a lower Stokes' shift can be considered fluorescence due to the radiative decay from the singlet excited state to the singlet ground state and the emission at 572 nm with a higher Stokes' shift value was the indication of phosphorescence as an emission phenomenon due to radiative decay from triplet excited state to singlet ground state. This exceptional dual emission property of [**L2Ir**] may be ascribed to increased π-conjugation of anthracene moiety in ancillary (N^N) ligand. The fluorescence lifetime of the complexes, [**L1Ir**], [**L2Ir**], and [**L3Ir**] were 0.056 μs, 0.049 μs, and 0.055 μs, respectively. The measurement of decay constant for the respective complexes showed high non-radiative decay constants ((K_{nr})$_{[L1Ir]}$ = 17.45, (K_{nr})$_{[L2Ir]}$ = 13.88, and (K_{nr})$_{[L3Ir]}$ = 16.76, respectively) as well as low radiative decay constants ((K_r)$_{[L1Ir]}$ = 0.54, (K_r)$_{[L2Ir]}$ = 6.53, and (K_r)$_{[L3Ir]}$ = 1.46, respectively). The significant fluorescence lifetime in the microsecond domain and high K_{nr} as compared to that of K_r also authenticated the feasibility of the phosphor-

Research Article
doi.org/10.1002/ejic.202400769

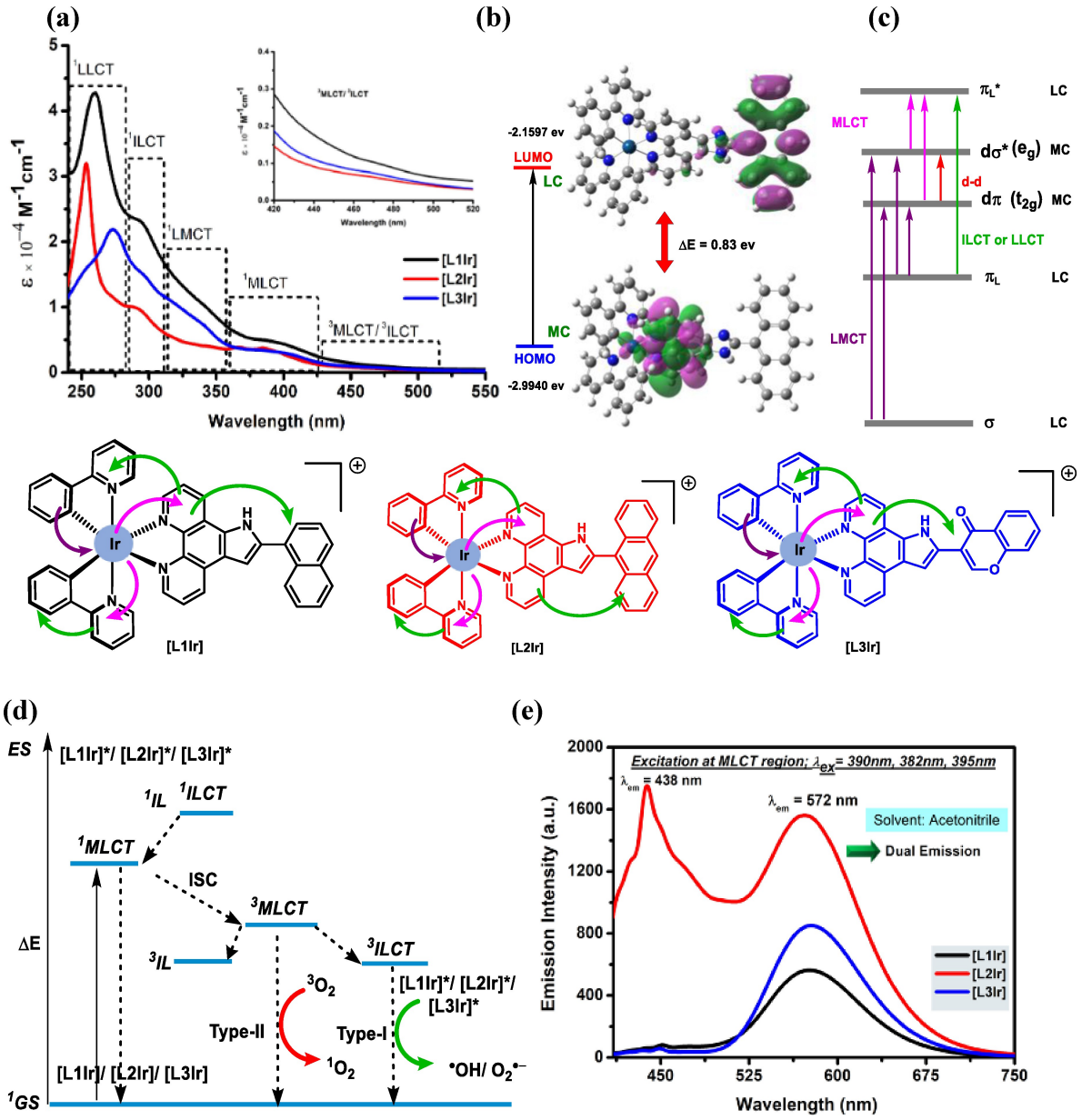

Figure 2. (a) Absorption spectra of [**L1Ir**], [**L2Ir**], and [**L3Ir**]; (b) HOMO to LUMO electronic transition considering the complex, [**L2Ir**]; (c) Probable electronic charge transfer transitions between different MOs associated with the respective complexes; (d) Jablonski diagram depicting the pathways of ROS generation; (e) Emission spectra of the complexes, [**L1Ir**], [**L2Ir**], and [**L3Ir**].

escence phenomenon upon excitation at the MLCT wavelength region. Interestingly, the high K_r of 6.53 for [**L2Ir**] in comparison to the other two complexes suggested the possibility of fluorescence as an emission process concomitant with the phosphorescence. The emission quantum yield for MLCT excitation, $(\Phi_f)_{MLCT}$ of each complex was determined considering rhodamine B as a standard. In reference to the quantum yield value of 0.31 of rhodamine B in aqueous solution, complexes, [**L1Ir**], [**L2Ir**], and [**L3Ir**] showed the quantum yields of 0.03, 0.32, and 0.08, respectively (Figure S13). The highest quantum yield value, large Stokes' shift, and significantly high non-radiative decay constant of [**L2Ir**] suggested that this complex was highly efficient among the other two complexes for taking part in phosphorescence promoting the generation of reactive oxygen species (ROS) in either of two ways: (1) energy transfer upon emission from low-lying excited ^{3}MLCT to ligand centered singlet ground state (^{1}LC) (conversion of $^3O_2 \rightarrow {}^1O_2$) or electron transfer upon emission from lowest-lying excited ^{3}ILCT to ground ^{1}LC state (generation of $O_2^{\bullet-}$, $^\bullet$OH, H_2O_2), described in Figure 2d during implementation of photodynamic therapy (PDT) under irradiation of visible light. The phosphorescence as an emission mechanism for all complexes can be rationalized as a consequence of spin-orbit coupling (SOC) and the presence of Ir(III) heavy metal triggering the rapid non-radiative inter-system crossing (ISC) to reach an excited triplet state from excited singlet state.[21,22]

Research Article
doi.org/10.1002/ejic.202400769

2.1.2. Electrochemical Characterisation by Cyclic Voltammetry

The measurement of redox efficiencies of complexes [**L1Ir**], [**L2Ir**], and [**L3Ir**] is very essential to rationalize their competency towards the formation of reactive oxygen species (ROS) undergoing various intracellular redox reactions. To comprehend the electron-transfer ability of these complexes, an electrochemical experiment was conducted using a highly conductive carbon black-modified glassy carbon electrode (GCE/CB) as the working electrode. Figure S14 depicts the cyclic voltammetry (CV) responses of [**L1Ir**], [**L2Ir**], and [**L3Ir**] adsorbed onto GCE/CB modified electrodes in phosphate buffer solution at pH 7.4. The redox potentials for the complexes [**L1Ir**], [**L2Ir**], and [**L3Ir**], were noted at −0.227 V, −0.293 V, and −0.159 V *vs* Ag/AgCl, respectively corresponding to the redox transitions of the $Ir^{III/IV}$ as an electron-transfer reaction. The electrode potential energy diagram also displays the reactive oxygen (ROS) generation capability of the complexes [**L1Ir**], [**L2Ir**], and [**L3Ir**] (Figure S14b).

2.2. DFT Study

Density Functional Theory (DFT) computations were conducted with the complex [**L2Ir**] as a representative of other complexes in a gas phase environment using the B3LYP exchange-correlation function as implemented in the Gaussian 09 W software suite. The LANL2DZ basis set was selected for these analyses.[23] The optimized structures of these complexes emphasizing key bond lengths, electron localization function (ELF), and covalent interactions between donor and acceptor atoms have been illustrated in Figure S15–S17. For the complex, [**L2Ir**], the bond angles C–Ir–N and N–Ir–N were found at 78.9° and 78.59°, respectively. The distances between the iridium and the nitrogen atoms of the donor ligands were as measured at 2.07 Å, 2.08 Å, and 2.16 Å, where the distances between iridium and co-ordinated carbon atoms of this cyclometallated complex were 2.02 Å, and 2. 04 Å. The molecular electrostatic potential map of this complex unveiled the different colour zones indicating the electron density and internal charge transfer that occurred in the complexes, where the red region indicated the high electron density, the blue zone indicated the low electron density, while the greenish blue colour pointed the positive region (Figure S16). In Figure S16a, a 3D map of the complex [**L2Ir**] displays non-covalent interactions, where a red-blue circle indicates the coordination bond, red spots stand for resonance, and green with golden tint stands for hydrogen bonds. Moreover, the RGD scatter plot and 2D map of the electron localization function (ELF) of the complex [**L2Ir**] reveal various bonding and non-bonding interactions that prevailed in this molecule (Figure S17a, b).

2.3. Solubility, Dark- and Photo-Stability

Envisioning the solubility of the complexes [**L1Ir**], [**L2Ir**], and [**L3Ir**] revealed that all complexes were highly soluble in DMSO and they had good solubility in methanol, ethanol, and acetonitrile whereas they were mostly insoluble in water medium. However, prior to the accomplishment of biological and photobiological studies, the determination of stability in dark as well as in light irradiation was a crucial factor in understanding the stability in different biological environments of cells and the photo durability of any photodynamic therapeutic agent in exposure to light. Therefore, we checked the stability of the complexes in 10% DMSO-PBS buffer solution, 1 mM GSH medium, DMEM medium, and 10% FBS solution at 25 °C and pH 7.4. This study demonstrated that all the complexes were highly stable in all tested mediums up to 72 hours of study (Figure S18–S21). Then we conducted the photostability study for all the complexes with the help of UV-visible spectroscopy.[24] Interestingly, all complexes exhibited good stability under visible light irradiation (400–700 nm, 10 Jcm^{-2}) for up to 45 minutes (Figure S22). We further investigated the photostability in time-dependent ^{1}H NMR spectroscopy and time-dependent HRMS using complex [**L2Ir**] as representative of other complexes. The photostability results in NMR spectroscopy and HRMS unveiled excellent photo endurance up to 45 minutes of study (Figure S23).[25]

2.4. Hemolysis Study

After ensuring the stability, the blood toxicity of the complexes was assessed by evaluating their hemocompatibility in terms of hemolysis study. Erythrocytes function as ideal osmometers, and their lysis can be triggered by variations in the blood's osmotic pressure and physical state. Hemoglobin is released when erythrocytes are destroyed, and when this hemoglobin is excreted in the urine, it is diagnosed as hemoglobinuria, or "blood poisoning." In this case, erythrocyte lysis serves as a reliable marker of the toxicity of any foreign substance to the blood cells. Moreover, erythrocyte bridging by metal complexes may be the cause of hemagglutination. Humans are severely affected by this impact, which causes blood cell blockage, blood osmolarity imbalance, and erythrocyte depletion that prevents proper blood function.[26] In order to inspect the hemolytic qualities of complexes [**L1Ir**], [**L2Ir**], and [**L3Ir**], a hemolysis study was performed at several concentrations (10, 25, 50 μg/ml). The positive and negative controls were saline solution, and Milli-Q water, respectively. After one hour of incubation with the complexes, it was observed that all three complexes were almost non-hemolytic up to 10 μg/ml (eqn. iii) according to the ISO/TR 7406.

2.5. Binding Propensity towards Human Serum Albumin (HSA)

Binding propensity between drugs and plasma proteins is an important fact in pharmacology and chemical biology. The binding of a drug with serum albumin, enhance the solubility as well as the transportation of drug in blood plasma reducing the toxicity of the bound drug. Human serum albumins (HSAs) are produced in liver and are the key globular proteins present

Research Article
doi.org/10.1002/ejic.202400769

in blood plasma of human. It has been studied that human serum albumin (HSA) is widely distributed in the cell's surroundings by creating a more active coordinate complex with the drug. This makes the precise admission of the drug easier into the cell after transportation through blood stream. Therefore, it is very crucial to rationalize the binding efficiencies of these complexes with HSA for confirming their facile transportation to the target cells.[27] HSA molecule inherits the fluorescence property due to the presence of tryptophan moiety or fluorescence resonance energy transfer (FRET) from tyrosine to tryptophan and it exhibits fluorescence emission at 330 nm upon excitation at 280 nm. Therefore, to comprehend the complex-HSA interaction phenomenon, we accomplished the emission quenching experiment upon gradual addition of the complexes, [**L1Ir**], [**L2Ir**] and [**L3Ir**] to the HSA solution at 25 °C and at constant pH of 7.4 (Figure S25). It was vividly observed that initial fluorescence intensity of the HSA was started to decline significantly upon gradual addition of the respective complexes with increased concentration (5–55 μM). The progressive lowering in fluorescence intensity firmly indicated the substantial interactions of the complexes with HSA, which was nicely corroborated by estimating the Stern–Volmer quenching constant (K_{HSA}), quenching rate constant (K_q), and binding constant (K) by applying the Equation (iv) and (v). The K_{HSA} values for the complexes [**L1Ir**], [**L2Ir**] and [**L3Ir**] were found to be $0.45\times10^6\ M^{-1}$, $0.83\times10^6\ M^{-1}$ and $0.27\times10^6\ M^{-1}$, respectively. The K_q values for these complexes were observed as $4.5\times10^{13}\ M^{-1}s^{-1}$, $8.3\times10^{13}\ M^{-1}s^{-1}$ and $2.7\times10^{13}\ M^{-1}s^{-1}$, respectively. Static quenching, efficient bimolecular quenching, and bimolecular binding with these molecules were all validated by finding K_q values greater than the highest value of dynamic quenching ($2.0\times10^{10}\ mol^{-1}s^{-1}$). The Scatchard Equation (vi) allowed us to calculate the total number of binding sites (n) and binding constants (K) for these complexes. In this study, we found that the complex [**L2Ir**] attained very strong binding efficacy with human serum albumin and facilitated the transportation of that complex towards the cell membrane. We further validated the binding propensity as well as the binding modes of [**L2Ir**] with HSA by dint of molecular docking (MD) study. The Autodock 4.2 computational program with the Lamarckian genetic algorithm (LGA) was used to study the blind docking experiment. The heart-shaped crystal structure of HSA (PDB ID: 1AO6) was taken from the Protein Data Bank, and then the structure was refined by using the online tool Swiss model. HSA is comprised of a single polypeptide chain with 585 amino acid residues, possessing three homologous α-helical domains: domain I (amino acid residues 1–195), domain II (amino acid residues 196–383), domain III (amino acid residues 384–585), and each domain contains two sub-domains, A and B (Figure 3). Different subdomains of human serum albumin are responsible for binding with innumerable endogenous and exogenous substances. The main binding sites of metallodrugs are located in between the subdomains IIA and IIIA of HSA, where metallodrugs interact with HSA in non-covalent ways, especially in the hydrophobic binding pockets lined by amino acid residues in subdomain IB. It was visualized that complex [**L2Ir**] was bound to HSA at the site below the subdomain IB, flanked by the subdomains IIA and IIIA. The significantly high binding energy of −11.11 kcal/mol pleasantly certified the experimental observation. The docked structure of [**L2Ir**] was stabilized by the various non-covalent interactions arising from alkyl and π-alkyl interactions with arginine residues (ARG-114, ARG-145), π-carbon interaction with arginine residue (ARG 186), amide-π stack interaction with histidine residue (HIS-146) of domain I along with π-σ interaction with isoleucine residue (ILE-142) and glycine residue (GLY 189). Moreover, amide-π stacking and π–π interactions of leucine residue (LEU-185) with the anthracenyl moiety stabilized the docked structure of [**L2Ir**] with HSA (Figure 3).[28]

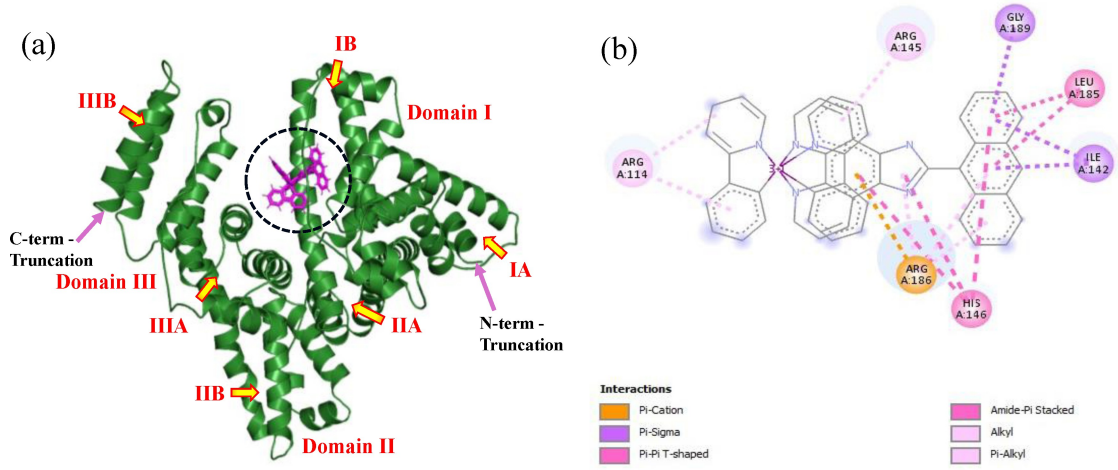

Figure 3. (a)
3D view of the best pose of the complex [**L2Ir**] within the hydrophobic pocket of HSA; (b) 2D representation indicating the multiple interactions of different amino acid residues of HSA with the complex [**L2Ir**].

2.6. Lipophilicity and Cellular Accumulation

Permeability is an essential characteristic of any drug candidate to comprehend the potential distribution of drug to the pharmacological target after considerable cellular accumulation by penetrating the cell membrane as well as to identify the ability of drug to traverse through the gastrointestinal (GI) tract. As the cell membrane consists of protein-lipid-protein bilayer, a suitable drug candidate should possess at least a threshold amount of lipophilicity (hydrophobicity) to be absorbed to the phospholipid membrane. Therefore, lipophilicity is an important parameter to measure the membrane permeability. It is mention-worthy; a balance between hydrophobicity and hydrophilicity is also required for intra-cellular interaction after successful membrane penetration. Consequently, we precisely studied the lipophilic competency of [**L1Ir**], [**L2Ir**], and [**L3Ir**] complexes to understand their membrane penetrating ability and considerable cellular accumulation. A lipophilicity study was performed in an n-octanol-water (PBS buffer) medium with the varied ratio of n-octanol and water to calculate the n-octanol/water partition coefficient ($P_{o/w}$) following the shake-flask method at 25 °C and pH 7.4 (Figure S26 a, b, c). Upon estimation of lipophilicity (Log $P_{o/w}$) for each of the three complexes, it was observed that complexes [**L1Ir**], [**L2Ir**], and [**L3Ir**] possessed the lipophilicity values of 1.12 ± 0.01, 1.22 ± 0.014, and 1.03 ± 0.169, respectively (Figure S26d). This consequence was also reflected in the cellular accumulation, which was also quantified by inductively coupled plasma mass spectrometry (ICP-MS) (Figure S26e).[26]

2.7. Photobiology

2.7.1. Cytotoxicity Under Dark and Light

The complexes [**L1Ir**], [**L2Ir**], and [**L3Ir**] were examined for in vitro cytotoxicity utilizing the 3-(4,5-dimethylthiazol-2-yl)-2,5-diphenyl-tetrazolium bromide (MTT) assay in TNBC cell line (MDA-MB-231) under dark and light exposure. The complex-treated cells were exposed to 4 mW cm^{-2} of yellow light at a dosage of 0–2 J cm^{-2} from a 400 W tungsten lamp equipped with a 500 nm long pass filter and a heat isolation filter for approximately 4 hours. Complexes [**L1Ir**], [**L2Ir**], and [**L3Ir**] exhibited a very nominal degree of dark cytotoxicity with IC_{50} values of 130.91 ± 2.72 μM, >300 μM, and >300 μM respectively (Table 1). In contrast, the complexes exhibit noteworthy IC_{50}, 2.68 ± 0.25 μM for [**L1Ir**] (through Type I and Type II PDT), 3.8 ± 0.34 μM for [**L2Ir**] (through Type I and Type II PDT), and 14.15 ± 0.05 μM for [**L3Ir**] (through only Type II PDT) when exposed to light. Even though the toxicity of [**L1Ir**] is the highest, the phototoxicity index (PI) of [**L2Ir**] ($PI^c_{[L2Ir]} = 78.94$) is much more prominent than [**L1Ir**], and [**L3Ir**] ($PI^c_{[L1Ir]} = 48.84$ and $PI^c_{[L3Ir]} = 21.20$), consequently making it the most potent in the series (Figure S27).

Table 1. Cytotoxicity of the Complexes [**L1Ir**], [**L2Ir**], and [**L3Ir**] against MDA-MB-231 under light and dark conditions.

Complexes	IC_{50} (μM)[a] MDA-MB-231		PI^c
	Dark	Light	
[L1Ir]	130.91 ± 2.72 μM	2.68 ± 0.25 μM	48.84
[L2Ir]	>300 μM	3.8 ± 0.34 μM	78.94
[L3Ir]	>300 μM	14.15 ± 0.05 μM	21.20

[a] IC50 is the concentration of the synthesized complexes at which 50% of cells undergo cytotoxic cell death under the treatment of a drug. PI^c (phototoxicity index) = ratio of IC_{50} in the dark to IC_{50} in light.

2.7.2. Photoinduced Singlet Oxygen($^1O_2$) Generation

The singlet oxygen ($^1O_2$) generation efficiency of a photosensitizer (PS) upon light irradiation is an essential factor to rationalize its capability for undergoing type II photodynamic therapy (PDT) at the target-site of cancer cells. Metal complexes as photosensitizer (PS), transfer energy to triplet molecular oxygen ($^3O_2$) during returning back to singlet ground state (^{1}GS) from excited triplet state (^{3}MLCT) and $^3O_2$ utilizes this energy for spin paring, which results in the formation of highly reactive singlet oxygen ($^1O_2$) as depicted in Figure 2d. Therefore, we used a standard protocol to quantify the singlet oxygen ($^1O_2$) generation efficiency of the complexes by UV-Visible spectroscopy upon photosensitization of the complexes [**L1Ir**], [**L2Ir**], [**L3Ir**] with respect to Rose Bengal (RB), an established photosensitized singlet oxygen generator using 1,3-diphenylisobenzofuran (DPBF) as $^1O_2$ sensitive photodegradable dye. As soon as $^1O_2$ starts to liberate in the solution at room temperature upon photoexcitation of the photosensitiser, the fluorescent probe (DPBF) reacts with $^1O_2$ and then immediately degrades to non-fluorescent 1, 2-dibenzoylbenzene *via* endoperoxide formation, which can be detected by the gradual decrease in optical density of DPBF in UV-Visible spectrum. In this study, we observed that absorbance of DPBF at 417 nm was gradually declined over a period of time in the precence of respective complexes under visible light irradiation (400–700 nm, 10 Jcm^{-2}) (Figure 4). This same analysis was also conducted for Rose Bengal to compare the $^1O_2$ generation competency of the complexes. The relative changes in absorbance of DPBF (A/A_0) was plotted against exposer times to visible light in second, where A_0 stands for absorbance of DPBF at zeroth time (t = 0 sec) and A is the absorbance of DPBF at a particular exposer time. The linearly declined plot (A/A_0 vs time) indicated the significant degradation of DPBF through conversion of $^3O_2$ to $^1O_2$ in favour of type II photodynamic process. Noteworthily, there was no such decrease in DPBF absorbance at 417 nm in the presence of the complexes in the dark condition under similar experimental conditions, which suggested the singlet oxygen generation was specifically under light condition but was reluctant to occur under dark condition. The calculated singlet oxygen quantum yields of complexes [**L1Ir**], [**L2Ir**], and [**L3Ir**] with reference to rose bengal [$(\Phi_\Delta) = 0.76$], were found to be 0.23, 0.26, and 0.29, respectively (eqn. (vii) and (viii)).

Research Article
doi.org/10.1002/ejic.202400769

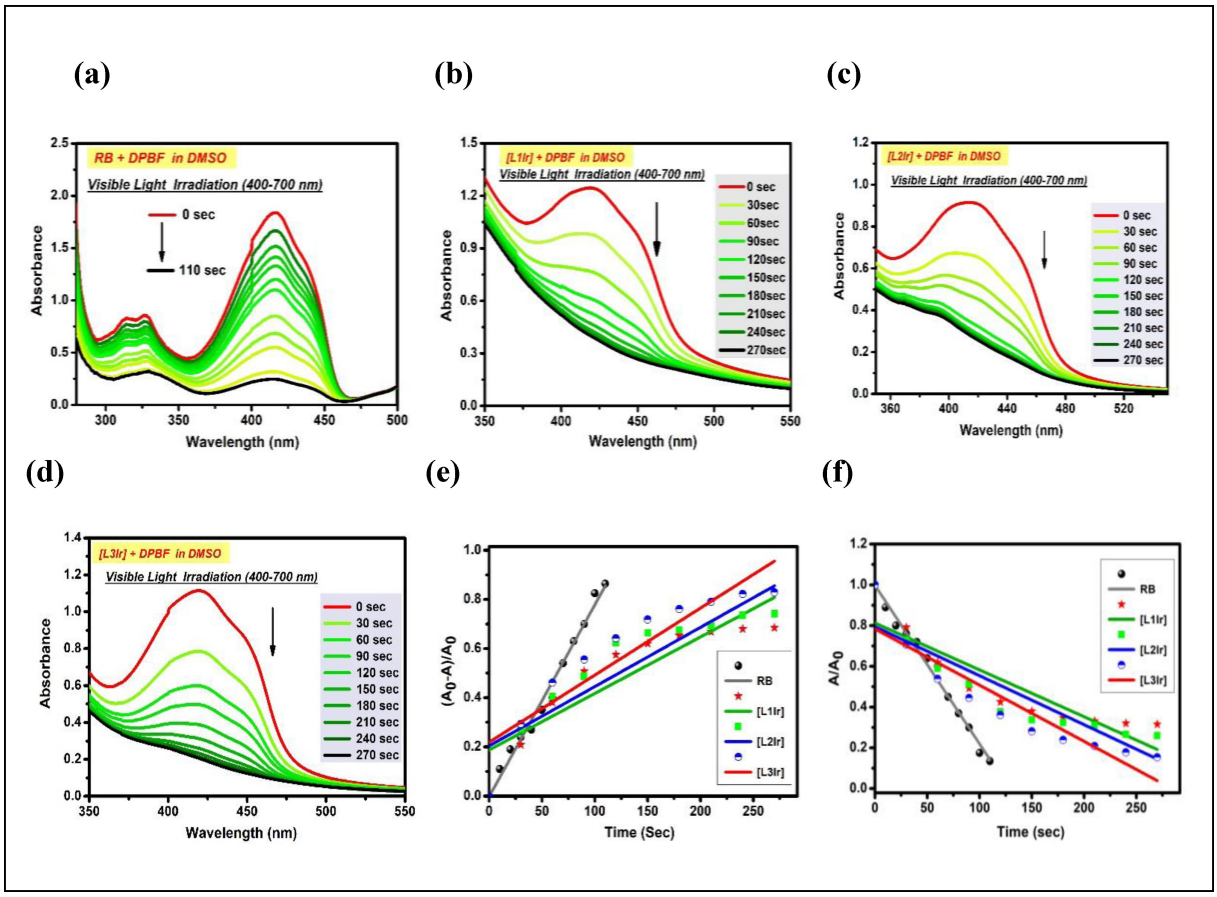

Figure 4. Singlet oxygen generation study by UV-visible spectroscopy in the presence of DPBF under visible light: For (a) Rose Bengal (RB); (b) Complex [**L1Ir**]; (c) Complex [**L2Ir**]; (d) Complex [**L3Ir**] at 298 K. (e) A competitive plot depicting singlet oxygen generation between Rose Bengal (RB) and complexes [**L1Ir**], [**L2Ir**], [**L3Ir**] as $(A_0–A)/A_0$ *vs* time in second; (f) Plots exhibiting the relative change in absorbance by DPBF for Rose Bengal and complexes [**L1Ir**], [**L2Ir**], [**L3Ir**] as (A/A_0) *vs* time in second at 417 nm.

Therefore, the substantial singlet oxygen quantum yield values of concerned complexes affirmed their probable abilities to take part in photodynamic therapy following type II pathway.[29]

2.7.3. Photocatalytic NADH Oxidation

Nicotinamide adenine dinucleotide (NAD) is the main coenzyme for regulating the redox reactions in cellular metabolic process. As the NADH (reduced form of NAD), plays an important role in the mitochondrial electron transport chain (ETC) system, the oxidation of NADH to NAD^+ interrupt the electron transport chain and thereby hinder the energy production during metabolic process, which results in the significant cellular damage. To certify the NADH oxidation capability of complexes [**L1Ir**], [**L2Ir**], and [**L3Ir**], we performed the UV-Visible absorption study following titration method. Interestingly, there was no significant change in absorption bands of the complex-NADH solution with time under dark condition. However, a significant increase in absorption band at $\lambda_{max} = 256$ nm was visualised for the successive production of NAD^+ due to gradual destruction of NADH upon irradiation of visible light (400–700 nm, 10 Jcm^{-2}) at a particular time interval in the solution of complex (25 μM) and NADH (150 μM) (Figure 5). This observation clearly indicated that visible light irradiation triggered the oxidation of NADH to NAD^+ catalysed by the activated complex. As a possible mechanism of photocatalytic NADH oxidation by the complexes [**L1Ir**], [**L2Ir**], and [**L3Ir**], it can be depicted that at first iridium in +3 state [Ir(III)] in each complex is excited to activated state [*Ir(III)] upon visible light irradiation. The activated *Ir(III) state in each complex releases electron and oxidised to Ir(IV) state. This unstable Ir(IV) state compel NADH to release an electron from N-centre of pyridine ring to form unstable $NADH^{\bullet+}$ intermediate. Then Ir(IV) takes a single electron to return to stable Ir(III) state and continue the catalytic cycle. The unstable $NADH^{\bullet+}$ releases one proton to form $NAD^{\bullet}$, which in turn releases electron to form ultimately NAD^+. In this way, the successive catalytic cycles triggered the conversion of NADH to NAD^+ upon visible light irradiation and we estimated the turn over frequencies (TOFs) for the conversion of NADH to NAD^+, where complex [**L2Ir**] showed the highest TOF of 37.82 $h^{\bullet 1}$ and complexes [**L1Ir**], [**L3Ir**] displayed the TOF values of 11.13 $h^{\bullet 1}$, 27.46 $h^{\bullet 1}$, respectively (Equation (viii)). Therefore, this study agreeably corroborates the photocatalytic capabilities of all the complexes attributing the complex [**L2Ir**] as the best photocatalyst for conversion of NADH to NAD^+, which in turn

Research Article
doi.org/10.1002/ejic.202400769

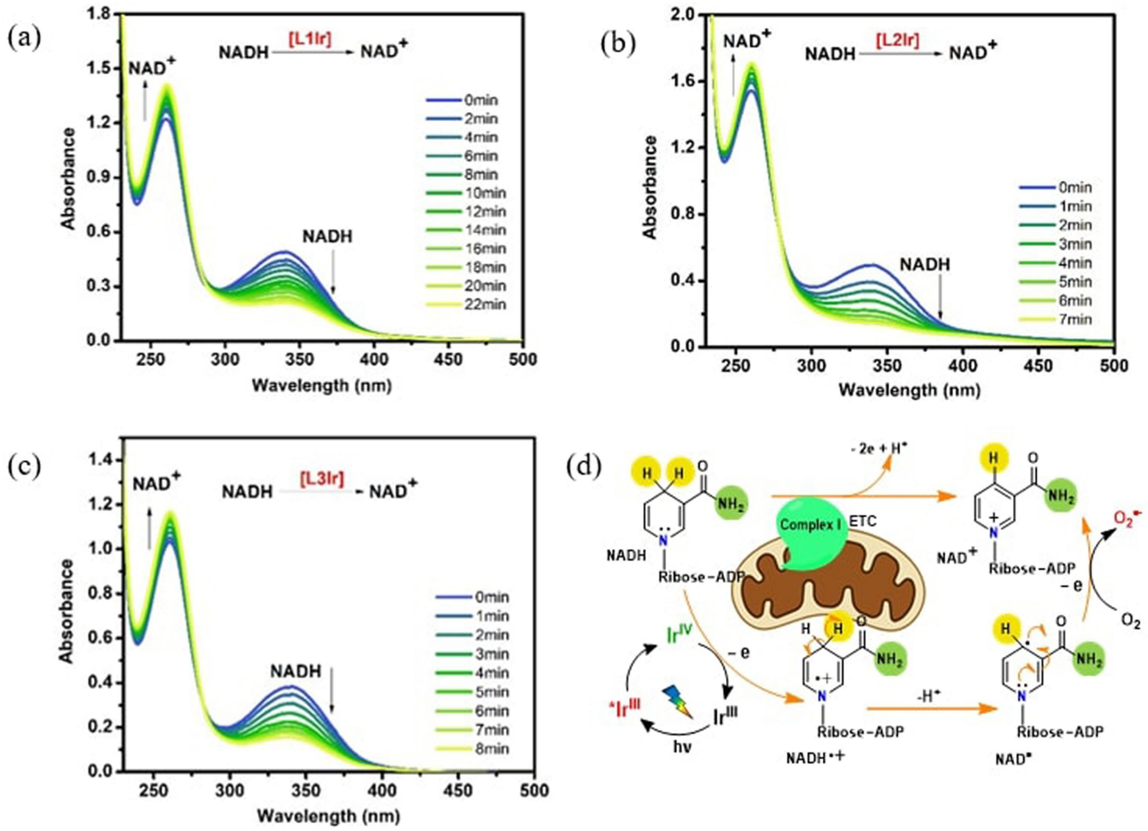

Figure 5. Photocatalytic oxidation of NADH (150 μM) exhibiting progressive changes in absorption band under visible light irradiation (400–700 nm, 10 Jcm^{-2}): By (a) Complex [**L1Ir**]; (c) Complex [**L2Ir**]; (d) Complex [**L3Ir**] at 298 K; (e) Plausible mechanism of catalytic photooxidation of NADH by complexes [**L1Ir**], [**L2Ir**], [**L3Ir**].

conveys the possibility of the formation of super oxide radical ($O_2^{\bullet-}$) as the reactive oxygen species (ROS) *via* reaction of molecular oxygen and free electron liberated in NADH to NAD^+ conversion [O_2-2e→$O_2^{\bullet-}$] (Figure 5).[30]

2.7.4. Reactive Oxygen Species Detection by TMB Assay

3,3′,5,5′-Tetramethylbenzidine (TMB) is a non-toxic and non-mutagenic colourless dye and its solution acquires a distinctive blue colouration upon oxidation. When TMB comes in contact with ROS, it produces TMB^+, which can be detected by a significant characteristic absorption band of TMB^+ at λ_{max} = 652 nm. Hence, the oxidation of TMB dye can be used as a detection tool to demonstrate the complexes' ability in the production of type I ROS species, *viz* hydroxyl radical (•OH) and superoxide radical ($O_2^{\bullet-}$) when subjected to light irradiation. At first, we obtained the absorption spectrum of TMB solution under light irradiation and then solutions of the complexes [**L1Ir**], [**L2Ir**], and [**L3Ir**] (25 μM) were exposed to visible light (400–700 nm, 10 Jcm^{-2}) for 60 minutes followed by incubation with 100 μM of TMB solution in PBS buffer medium at 25 °C (pH = 7.4). After that, we immediately checked the absorption spectrum of the complex-TMB mixture (Figure S28). The emergence of a new absorption band at 652 nm was the indication for TMB^+ formation upon oxidation of TMB by the type I ROS produced under light irradiation (Figure S28b). Therefore, this experiment supports the ability of the complexes for type I ROS production, which may also involve the type I pathway of photodynamic therapy to exterminate triple negative breast cancer.[31]

2.7.5. GSH Depletion Study

Cancer cells are sheltered by the shielding effect of the high antioxidant content and hence the suppression of antioxidant system opens an easy and effective way to attack cancer cells *via* a ROS-mediated mechanism. Glutathione (GSH) is regarded as the most prevalent endogenous antioxidant, which possess the main source of nonprotein thiol groups in cells and maintain the redox homeostasis in cells. In this regard, breaking of redox homeostasis *via* intracellular GSH depletion finds an inevitable aspect to make the cancer cells more vulnerable to ROS harvesting metallodrugs. Therefore, we tested the capability of three complexes [**L1Ir**], [**L2Ir**], and [**L3Ir**] for depletion of intracellular glutathione level as this is very crucial analysis to support the ROS-mediated DNA damage as one of the important pathways of cancer cell death. We accomplished this study in UV-Visible absorption spectroscopy using the Ellman's reagent, 5, 5-dithiobis-(2-nitrobenzoic acid) (DTNB) as a specific detector of thiol group in a sample. DTNB possesses the

characteristic absorption band at around $\lambda_{max} = 325$ nm. When DTNB comes in contact with GSH, GSH readily reacts with DTNB and cleaves the S–S linkage forming the oxidized GS-TNB adducts. Consequently, TNB is set free in the solution, and it exhibits the absorption band at $\lambda_{max} = 412$ nm. Therefore, gradual shifting of λ_{max} from 325 nm to 412 nm is an indication of reaction of free GSH with DTNB. The steady increase in absorption intensity at 412 nm measures the higher rate of TNB formation and hence the concentration of GSH in solution. Initially, we followed the titration method to quantify the total GSH content in the sample keeping the DTNB concentration fixed at 55 μM and made a standard curve by plotting the different absorption values at 412 nm versus known concentration of GSH (0–60 μM) and we obtained a linear curve for further analysis of GSH concentration in unknown sample (Figure S29a, b). In the next step, we studied the GSH depletion capability of the respective complexes by incubating each complex (50 μM) with 55 μM DTNB and 55 μM GSH for 2 minutes in DMSO-PBS buffer medium at 25 °C (pH 7.4). From the respective absorbance values at 412 nm for the complexes [**L1Ir**], [**L2Ir**], and [**L3Ir**], we quantified the corresponding free GSH concentration from the standard curve and then calculated the amount of depleted GSH for each complex. The calculated result showed that [**L1Ir**], [**L2Ir**], and [**L3Ir**] depleted the GSH by 37.5 μM, 40.5 μM and 29 μM, respectively (Figure S30). These findings demonstrated the high competency of the metal complexes to destroy the cancer cells by reactive oxygen species hindering the activity of intracellular GSH.[26]

2.7.6. Study of DNA Impairment Under Dark and Light

Deoxyribonucleic acid (DNA) plays a pivotal role in regulating cellular growth, survival, and reproduction as well as in carrying genetic material from generation to generation. Therefore, DNA damaging strategy has become a topic of interest in this present work to develop a new approach to treating triple-negative breast cancer. Here, we have tried to develop a TNBC preventive therapeutic pathway through measuring the DNA damaging potential of imidazophenenthroline-based simple and small cyclometallated Ir(III)-complexes upon generation of singlet oxygen or type I reactive oxygen species (ROS). To scale the propensity of complex-DNA interaction and ROS-mediated DNA damage, we performed the UV-visible absorption study in the presence and absence of visible light irradiation as UV–Vis spectroscopy offers the simplest and highly insightful technique for comprehending the complex-DNA interaction. In this study, we periodically added the calf thymus DNA (ct-DNA) solution with increasing concentration (0 μM→20 μM for [**L1Ir**]; 0 μM→ 30 μM for [**L2Ir**]; 0 μM →35 μM for [**L3Ir**]) to the fixed concentration of the complexes (25 μM) at 25 °C. Consequently, we observed significant hypochromism at π–π*, LMCT and MLCT regions in the absorption spectra of the complexes [**L1Ir**], [**L2Ir**], and [**L3Ir**] (Figure S30), which can be considered as a result of the lowering of absorption intensity upon accumulation of π-electrons into the DNA base pair.[32] In association with the hypochromic effect for all complexes, a considerable bathochromic shift was only observed for complex [**L1Ir**] at $\lambda_{max} = 258$ nm and a decent bathochromic shift for complex [**L3Ir**] at $\lambda_{max} = 272$ nm, whereas bathochromic was not visualized in the absorption spectrum of complex [**L2Ir**]. The bathochromic shift in the absorption spectrum of [**L1Ir**] at π–π* region can be attributed to the fact of overlapping the vacant π orbitals of this complex with the filled π orbitals of DNA bases diminishing the overall energy gap of π→π transition, which leads to the shift of absorbance at longer wavelength (bathochromic shift). The significant hypochromic shift manifested sturdy intercalative interactions for all complexes, while complex [**L1Ir**] exhibited electrostatic as well as intercalative interactions with ct-DNA. The calculation of intrinsic binding constants (K_b) (eqn. ix) displayed the values as 1.59×10^5 M^{-1}, 1.45×10^5 M^{-1}, and 0.73×10^5 M^{-1}, respectively for complexes [**L1Ir**], [**L2Ir**], and [**L3Ir**] (Figure 6a). The intrinsic binding constant values in the 10^3 to10^6 order strongly support favour of the intercalative mode of binding interaction between complexes and DNA,[33] which was also validated by the negative values of Gibbs free energy [$(\Delta G_o)_{[L1Ir]} = -29.68$ KJ/mol; $(\Delta G_o)_{[L2Ir]} = -29.44$ KJ/mol and $(\Delta G_o)_{[L1Ir]} = -27.74$ KJ/mol] indicating the spontaneous drug-DNA intercalation process.

An EtBr displacement assay was also performed using a spectrofluorometer to rationalize the intercalative mode of interaction of the synthesized complexes with ct-DNA. After addition to ct-DNA, EtBr exhibited significant fluorescence at $\lambda_{ems} = 604$ nm upon excitation at λ_{abs} 485 nm, as a result of its intercalative manner of interacting with a DNA base pair. With each subsequent rise in the concentration of the metal complexes, the fluorescence intensity of the EtBr-DNA adduct was steadily reduced (hypochromic nature). It implies that EtBr is successively removed from the EtBr-DNA adduct, upon intercalative interaction between DNA and the metal complexes. We obtained the *Kapp* values as 2.67×10^6 M^{-1}, 3.2×10^6 M^{-1}, and 1.45×10^6 $M^{-1}$for complexes [**L1Ir**], [**L2Ir**] and [**L3Ir**], respectively using Equation (x) under the condition of 50% reduction of emission intensity. The Stern-Volmer quenching constant (K_{SV}) values of complexes [**L1Ir**], [**L2Ir**] and [**L3Ir**], were determined as 3.8×10^4 M^{-1}, 3.9×10^4 M^{-1} and 1.5×10^4 M^{-1}, respectively (Equation (xi)). The highest K_{app} value of complex [**L2Ir**] revealed the most powerful intercalative nature of this complex compared to [**L1Ir**], and [**L3Ir**]. We also calculated the C_{50} values for the complexes by plotting the % fluorescence *vs* concentration of complexes to measure their relative intercalative competency in interaction with DNA. In Figure 6b, we observe the C_{50} values as 28.84 μM for [**L1Ir**], 24.06 μM for [**L2Ir**], and 50.71 μM for [**L3Ir**]. The lowest C_{50} value of [**L2Ir**] strongly corroborates the previous findings in support of the most intercalative nature of the complex [**L2Ir**]. Therefore, the intercalative mode of complex-DNA interaction can be considered the predominant mechanism for DNA damage in dark conditions.

After the comprehensive insight into the DNA damaging capabilities of the complexes in the absence of light, we investigated the visible light-inspired DNA photocleavage in UV-visible spectroscopy. It was observed that complexes were capable of progressively damaging the DNA upon irradiation of

Research Article
doi.org/10.1002/ejic.202400769

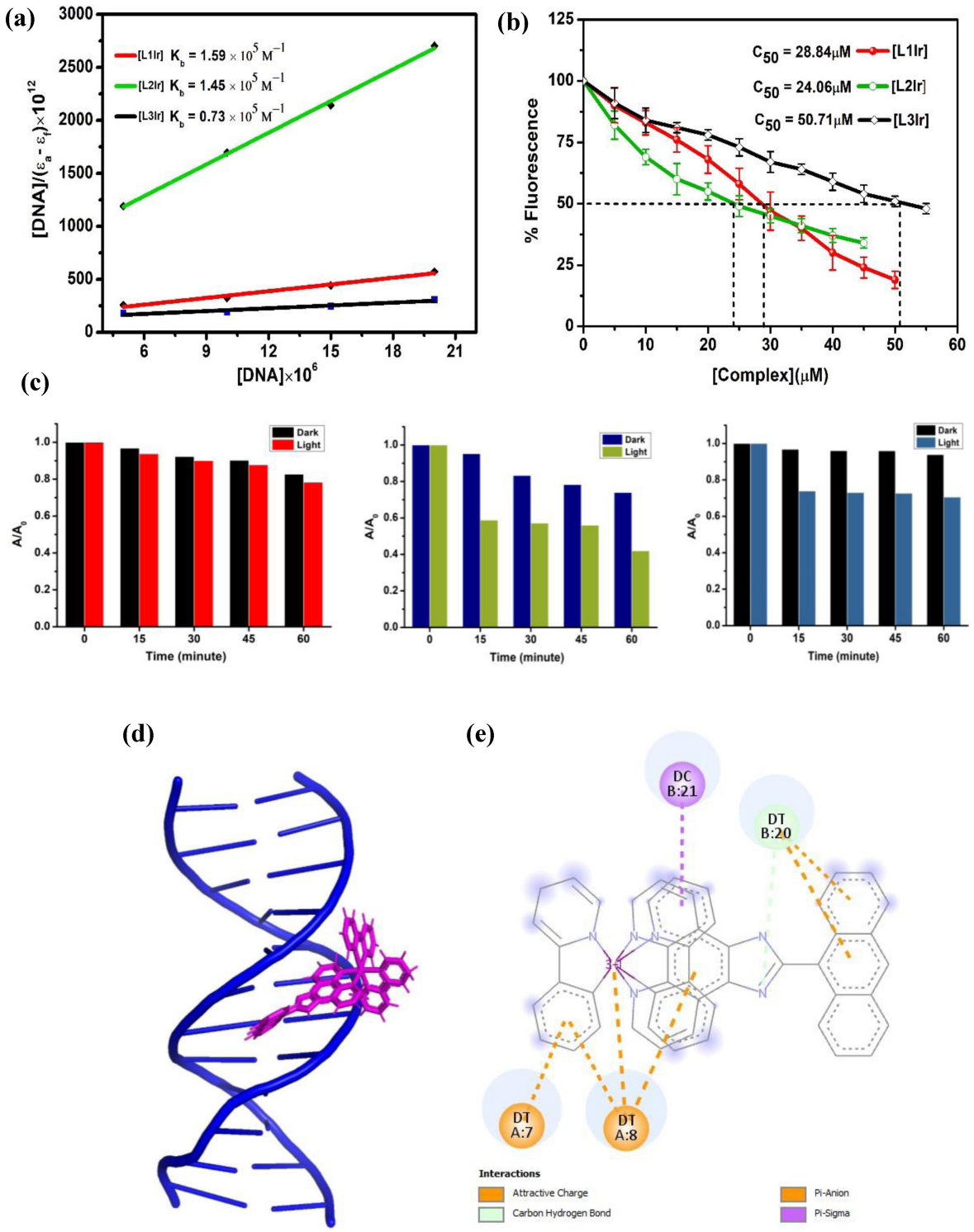

Figure 6. (a) Complex-DNA interaction study by UV-Vis spectroscopy and respective K_b values for complexes [**L1Ir**], [**L2Ir**], and [**L3Ir**]; (b) Ethidium bromide (EtBr) displacement by relative quenching of fluorescence intensities and respective C_{50} values for complexes [**L1Ir**], [**L2Ir**] and [**L3Ir**]. (c) Comparative study of DNA photo-cleavage by UV-Vis spectroscopy. (d) 3D view of [**L2Ir**]-DNA interaction; (e) 2D view of [**L2Ir**]-DNA interaction.

visible light (400–700 nm, 10 Jcm^{-2}) for 60 minutes. The relative competency of DNA photocleavage was also identified by plotting A/A$_0$ *vs* time concerning the DNA damage in dark conditions (Figure 6c). The A/A$_0$ *vs* time plot revealed that complex [**L2Ir**] was highly capable of damaging DNA under light irradiation in comparison to the other two complexes through the generation of toxic reactive oxygens species (ROS).

To ratify the complex-DNA interaction theoretically, we also performed a molecular docking study with the best DNA-damaging complex [**L2Ir**]. In theoretical outlook, complex [**L2Ir**]

Research Article
doi.org/10.1002/ejic.202400769

comes out as the robust DNA binding moiety with a remarkable binding constant of −10.4 kcal/mol by undergoing different interactions (Figure 6e).

2.8. Proposed Mechanism of Cell Death by PDT Based on the Obtained Result

Based on the obtained result we delineated a clear mechanism of DNA impairment in favor of triple-negative breast cancer cell death (Figure 7). The redox potential of the complexes showed that they can fluctuate from +3 to-4 oxidation state depending upon the conditions and the complexes can generate singlet oxygen as well as superoxide or hydroxyl radicals upon irradiation of visible light (400–700 nm, 10 Jcm^{-2}). Therefore, we have postulated that visible light irradiation may unveil two pathways (type I and type II) of photodynamic therapy, where the type II mechanism predominates more than type I. In the type II process, significant DNA impairment occurs due to the formation of 8-oxo-deoxyguanosine (8-Oxo-dG) from the deoxyguanosine moiety by the toxic impact of singlet oxygen, which indicates the damage of guanine base in DNA as depicted in Figure 7. On the other hand, complexes also show the capability of energy transfer to generate other reactive oxygen species *via the* type I pathway. As a consequence, the effect of both mechanisms triggers DNA impairment leading to apoptosis of triple-negative breast cancer cells.

3. Conclusions

In conclusion, we can depict that we have successfully synthesized and characterized the complexes [**L1Ir**], [**L2Ir**], and [**L3Ir**]. The meticulous investigations have revealed that complexes are eligible to release reactive oxygen species upon visible light irradiation instigating the damage of DNA. The complexes have shown remarkable photostability, which can help them to withstand visible light. The phototoxicity index revealed that complex [**L2Ir**] is more phototoxic compared to the others. The human serum albumin interactions and DNA binding studies also justify the best efficiency of the complex [**L2Ir**] towards biomolecular interactions.

Experimental Section

Materials and Methods. In this study, high-quality reagents and solvents of commercial grade were employed. All chemicals and biochemical substances were sourced from Sigma-Aldrich Chemicals Limited, Spectrochem, TCI Chemicals, and E-Merck. Cell lines utilized in the experiments were obtained from NCCS, Pune. A Bruker DPX spectrometer with high power (400 MHz) was employed to record all of the NMR spectra, with tetramethyl silane (TMS) serving as the standard. A TDS conductometer-307 was used to measure the complexes' experimental conductivity. A Shimadzu Affinity FT-IR spectrometer was utilized to record the complexes' infrared (IR) spectra across the range of 4000–400 cm^{-1}. JASCO 8440 fluorescence spectrophotometer with a xenon lamp was selected for the fluorescence experiment and a JASCO V-730 spectrophotometer with a 1 cm quartz cell was utilized for the UV–visible absorption experiment. An Elisa reader and 96 wallplates were utilized for the MTT assay. MDA-MB-231 (TNBC) cells were purchased from the National Centre for Cell Sciences (NCCS, Pune, India). Cell culture supplies such as Dulbecco's Modified Eagle's Medium (DMEM) along with 1% penicillin, streptomycin, and 1% Glutamax, were procured from Gibco. Fetal Bovine Serum (FBS), and Dimethyl Sulfoxide (DMSO), antibiotic mixture, Trypsin, Reduced Glutathione, DTNB were purchased from Hi-Media laboratories in Mumbai.

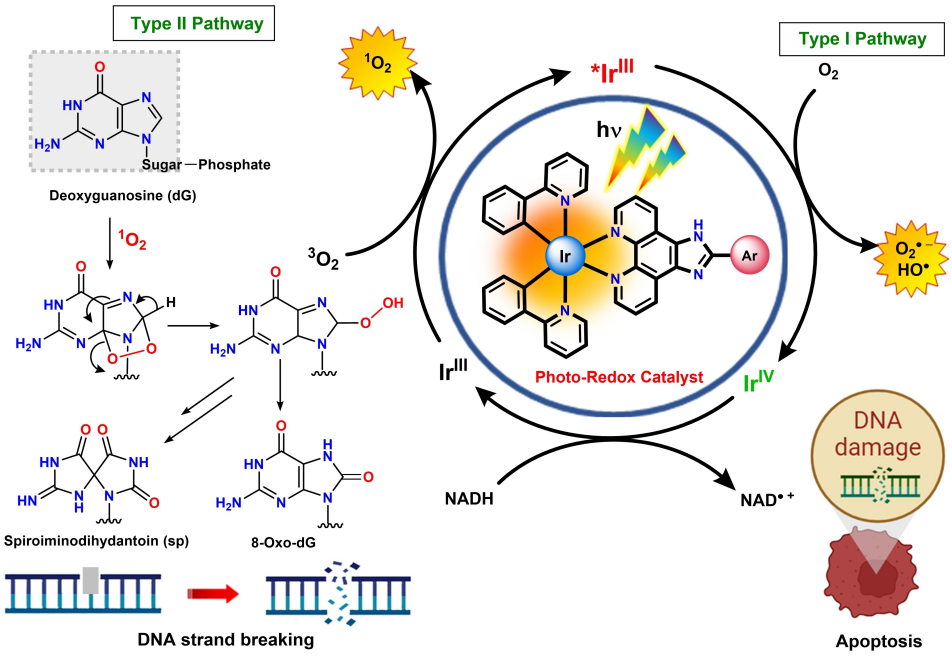

Figure 7. Proposed mechanism of DNA impairment by visible light-induced ROS generation.

Research Article
doi.org/10.1002/ejic.202400769

General Synthetic Procedure for the Preparation of Iridium(III)-Cyclometallated Imidazophenanthroline Complexes ([L1Ir], [Ir2Ir], [L3Ir])

30 mg (0.02 mmol, 1 equiv.) of bright yellow coloured iridium precursor ([**IrCP**]) was taken in a pear-shaped flask and it was dissolved properly in 10 ml of 4: 1 toluene/methanol solvent mixture to get a clear yellowish solution. Then 2.1 equivalents of the previously prepared pure ligand (**L1**/**L2**/**L3**) were added to the solution of iridium precursor ([**IrCP**]) and sonicated for 5 minutes to get a clear brownish-coloured solution upon thoroughly mixing the reactants. Thereafter, the reaction mixture was refluxed for 6 h in N_2-atmosphere at 120 °C. The progression of the reaction was periodically monitored by thin-layer chromatography (TLC) using 100% methanol as a solvent system. At around 6 h of reflux, we observed a significant change in the colour of the reaction mixture from pale brown to dark brown, and the completion of the reaction was confirmed by re-performing the TLC. After cooling the reaction mixture at room temperature, the product was seen to be precipitated out. Then, we obtained the crude product after filtration. The crude product was repeatedly washed with hexane as well as hexane-ethyl acetate mixture (3:1) 5–6 times to remove impurities and the purity of the product was checked by performing the TLC. The cleaned product was then dried and subjected to recrystallization from methanol/diethyl ether to obtain more purified product. The crystalline product of each complex was weighed in a weighing balance and the %yield was calculated. In due course, we obtained the deep yellow to reddish brown coloured crystals of complexes [**L1Ir**], [**L2Ir**], and [**L3Ir**] with high yields (91–97%). The structures of all the complexes were assured by ^{1}H, ^{13}C NMR, FT-IR spectroscopy, and HRMS. The purity of the complexes was scrutinized by ultraperformance liquid chromatography (UPLC) as well as with C, H, N analysis.

*[**L1Ir**]*. 48 mg (0.054 mmol, 97%); M_r ($C_{45}H_{30}N_6IrCl$) = 882.43 g/mol; Anal. calcd for $C_{45}H_{30}N_6IrCl$: C 61.25, H 3.43, N 9.52; found: C 61.23, H 3.48, N 9.48; Yield: 97%; Colour: Deep Yellow; Mp: 220–225 °C; R_f (100% methanol): 0.22; UPLC purity (61.9%, eluent: 50% H_2O/ACN, R_t: 2.087 min); ^{1}H NMR (DMSO-d_6, 400 MHz): δ 9.29 (s, 2H, ArH), 9.02 (d, J = 7.6 Hz, 1H, ArH), 8.28 (d, J = 8. 4 Hz, 3H, ArH), 8.21–8.12 (m, 4H, ArH), 8.11–8.08 (m, 3H, ArH), 7.97 (d, J = 7.6 Hz, 2H, ArH), 7.89 (t, J = 7.2 Hz, 2H, ArH), 7.78 (t, J = 8.0 Hz,1H, ArH), 7.72–7.65 (m, 2H, ArH), 7.54 (d, J = 5.6 Hz, 2H, ArH), 7.08 (t, J = 6.8 Hz, 2H, ArH), 7.02–6.94 (m, 4H, ArH), 6.32 (d, J = 7.2 Hz, ArH); ^{13}C NMR (DMSO-d_6, 100 MHz): δ 168.5, 151.7, 143.7, 137.9, 136.2, 134.2, 131.9, 130.9, 130.7, 130.6, 130.0, 129.1, 128.5, 126.9, 126.4, 125.9, 124.9, 123.7, 123.0, 122.8, 122.1, 121.3, 118.4; IR (cm^{-1}, KBr): ν 3362 (medium, N–H stretching), 3063 (weak, Arm sp2 C–H stretching), 2910 (weak, sp3 C–H stretching), 1580 (strong, Arm C=C stretching), 1472 (strong, C–N stretching), 1406 (strong, C=C bending), 1167 (C=C bending), 762 (strong, C–H bending); HRMS (MeOH) *m/z:* 847.2162 $[M–Cl]^+$.

*[**L2Ir**]*. 50 mg (0.054 mmol, 96%); M_r ($C_{49}H_{32}N_6IrCl$) = 932.49 g/mol; Anal. calcd for $C_{49}H_{32}N_6IrCl$: C 63.11, H 3.46, N 9.01; found: C 63.12, H 3.45, N 8.95; Yield: 96%; Colour: Brown; Mp: 235–240 °C; R_f (100% methanol): 0.21; UPLC purity (96.9%, eluent: 50% H_2O/ACN, R_t: 2.883 min); ^{1}H NMR (DMSO-d_6, 400 MHz): δ 9.14 (d, J = 8.0 Hz, 2H, ArH), 8.87 (S, 1H, ArH), 8.29–8.23 (m, 4H, ArH), 8.14 (d, J = 4.8 Hz, 2H, ArH), 8.04–8.00 (m, 2H, ArH), 7.98 (d, J = 7.6 Hz, 2H, ArH), 7.91 (t, J = 7.2 Hz, 2H, ArH), 7.86 (d, J = 9.2 Hz, 2H, ArH), 7.59 (t, J = 6.4 Hz, 4H, ArH), 7.49 (t, J = 8.0 Hz, 2H, ArH), 7.09–7.03 (m, 4H, ArH), 6.97 (t, J = 7.6 Hz, 2H, ArH), 6.35 (d, J = 7.6 Hz, 2H, ArH); ^{13}C NMR (DMSO-d_6, 100 MHz): δ 168.5, 154.8, 150.9, 149.2, 146.6, 142.9, 141.0, 137.8, 136.7, 134.2, 133.8, 131.9, 131.0, 128.4, 126.8, 124.9, 123.1,122.2, 119.5; IR (cm^{-1}, KBr): ν 3360 (weak, N–H stretching), 3044 (weak, Arm sp2 C–H stretching), 2915 (weak, sp3 C–H stretching), 1602 (strong, Arm C=C stretching), 1472 (strong, C–N stretching), 1163 (medium, C=C bending), 1027 (medium, C=C bending), 755 (strong, C–H bending); HRMS (MeOH) *m/z:* 897.2318 $[M–Cl]^+$.

*[**L3Ir**]*. 46 mg (0.051 mmol, 91%); M_r ($C_{44}H_{28}N_6O_2IrCl$) = 900.40 g/mol; Anal. calcd for $C_{44}H_{28}N_6O_2IrCl$: C 58.69, H 3.13, N 9.33; found: C 58.68, H 3.12, N 9.40; Yield: 91%; Colour: Reddish Brown; Mp: 215–220 °C; R_f (100% methanol): 0.26; UPLC purity (99.5%, eluent: 50% H_2O/ACN, R_t: 2.741 min); ^{1}H NMR (DMSO-d_6, 400 MHz): δ 8.33 (d, J = 7.6 Hz, 1H, ArH), 8.28 (d, J = 8.0 Hz, 2H, ArH), 8.16 (brs, 2H, ArH), 8.07–8.10 (m, 2H, ArH), 7.97 (t, J = 8.0 Hz, 4H, ArH), 7.88 (t, J = 8.0 Hz, 4H, ArH), 7.68 (t, J = 7.6 Hz, 1H, ArH), 7.52 (d, J = 6.0 Hz, 2H, ArH), 7.07 (t, J = 7.6 Hz, 2H, ArH), 7.00–6.95 (m, 5H, ArH), 6.31 (d, J = 7.6 Hz, 2H, ArH); ^{13}C NMR (DMSO-d_6, 100 MHz): δ 168.1, 158.5, 148.4, 148.2, 143.6, 138.0, 134.3, 131.9, 130.9, 126.6, 125.8, 124.9, 123.1, 122.8, 119.7; IR (cm^{-1}, KBr): ν 3058 (weak, Arm sp2 C–H stretching), 2922 (weak, sp3 C–H stretching), 2030 (medium, C=O stretching), 1894 (), 1603 (medium, Arm C=C stretching), 1479 (medium, C–N stretching), 1275 (strong, C=C bending), 1120 (C=C bending), 761 (strong, C–H bending); HRMS (MeOH) *m/z:* 865.1904 $[M–Cl]^+$.

4. Supporting information Summary

[†]^{1}H,^{13}C NMR, FT-IR spectra, UPLC, HRMS of all compounds; Quantum yield plot; DFT computed optimized structure; CV responses; Stability study plots; %Hemolysis plots, HSA binding plots; Representative diagram of lipophilicity; ICP-MS Analysis; plots of NADH oxidation, TMB oxidation plots; plots for glutathione depletion, plots of DNA binding, EtBr quenching; Experimental Procedure.

5. Abbreviations

TLC	thin-layer chromatography
FT-IR	Fourier transform-infra red
HRMS	high-resolution mass spectrometry
ILCT	intra-ligand charge transfer
LLCT	ligand-ligand charge transfer
LMCT	ligand-metal charge transfer
MLCT	metal-ligand charge transfer
CV	cyclic voltammetry
DFT	density functional theory
DMSO	dimethyl sulphoxide
DMF	dimethyl formamide
PBS	phosphate buffer saline
FBS	fetal bovine serum
DMEM	dulbecco's modified eagle's medium
HSA	human serum albumin
MTT	3-(4,5-dimethylthiazol-2-yl)-2,5-diphenyltetrazolium bromide
NADH	nicotinamide adenine dinucleotide (reduced)
TMB	3,3′,5,5′- Tetramethylbenzidine
GSH	glutathione
DTNB	5, 5-dithiobis-(2-nitrobenzoic acid)
ct-DNA	calf-thymus DNA
EtBr	ethidium bromide.

Research Article
doi.org/10.1002/ejic.202400769

6. Funding Sources

DST CRG project grant (CRG/2021/002267), Government of India. VIT SEED funding.

Author Contributions

The project was developed and supervised by PP (Vellore Institute of Technology). Synthesis, characterization, analytical, and preliminary biological tests were executed by SG (Vellore Institute of Technology).

Acknowledgements

The authors are grateful to the Department of Science and Technology (DST), Government of India, for supporting the work through the DST-SERB CRG project grant. The authors thank the Vellore Institute of Technology (VIT) for arranging VIT SEED funding. The authors are also grateful to the Department of Science and Technology, New Delhi, India, for providing financial support to acquire "Inductively Coupled Plasma Mass Spectrometry (ICP-MS)" through "Promotion of University Research and Scientific Excellence (PURSE)" under Grant No. SR/PURSE/2020/34 (TPN 56960) and carry out the work.

Conflict of Interests

"There are no conflicts to declare".

Data Availability Statement

The data that supports the findings of this study are available in the supplementary material of this article.

Keywords: Triple Negative Breast Cancer · Photodynamic Therapy · ROS · DNA Cleavage · NADH Oxidation · GSH Depletion · Cell Death

[1] B. Liu, H. Zhou, L. Tan, K. T. H. Siu, X.-Y. Guan, *Signal Trans. Targeted Ther.* **2024**, *9*, 175.
[2] S. Łukasiewicz, M. Czeczelewski, A. Forma, J. Baj, R. Sitarz, A. Stanisławek, *Cancers* **2021**, *13*, 4287.
[3] P. Khongorzul, C. J. Ling, F. U. Khan, A. U. Ihsan, J. Zhang, *Mol. Cancer Res. MCR* **2020**, *18*, 3–19.
[4] a) N. M. Almansour, *Front. Mol. Biosci.* **2022**, *9*, 836417; b) R. L. Siegel, K. D. Miller, N. S. Wagle, A. Jemal, *Cancer J Clin.* **2023**, *73*, 17–48; c) H. Sung, J. Ferlay, R. Siegel, M. Laversanne, I. Soerjomataram, A. Jemal, F. Bray, *Cancer J Clin.* **2021**, *71*, 209–249.
[5] S. Zhu, Y. Wu, B. Song, M. Yi, Y. Yan, Q. Mei, K. Wu, *J. Hematol. Oncol.* **2023**, *16*, 100.
[6] L. Yin, J.-J. Duan, X.-W. Bian, S.-C. Yu, *Breast Cancer Res.* **2020**, *22*, 61.
[7] O. Obidiro, G. Battogtokh, E. O. Akala, *Pharmaceutica* **2023**, *15*, 1796.
[8] J. Wang, S.-G. Wu, *Breast Cancer* **2023**, *15*, 721–730.
[9] a) Q. Zhang, Q.-B. Lu, *Sci. Rep.* **2021**, *11*, 788; b) R. Oun, Y. E. Moussa, N. J. Wheate, *Dalton Trans.* **2018**, *47*, 6645–6653.
[10] N. Alvarez, A. Sevilla, *Int. J. Mol. Sci.* **2024**, *25*, 1023.
[11] D. E. Dolmans, D Fukumura, R. K. Jain, *Nat. Rev. Cancer* **2003**, *5*, 380–387.
[12] P. Agostinis, K. Berg, K. A. Cengel, T. H. Foster, A. W. Girotti, S. O. Gollnick, S. M. Hahn, M. R. Hamblin, A. Juzeniene, D. Kessel, M. Korbelik, *CA: a Cancer J Clinicians* **2011**, *4*, 250–281.
[13] N. Sobhani, A. A. Samadani, *J Egypt. National Cancer Institute* **2021**, *33*, 1–13.
[14] S. Abbas, I. U. D. Din, A. Raheel, *Appl. Organometallic Chem.* **2020**, *3*, 5413.
[15] L. C. C. Lee, K. K. W. Lo, *J. Am. Chem. Soc.* **2022**, *32*, 14420–14440.
[16] Z. T. Chu, N. Xu, Y. Su, H. Fang, Z. Su, *Dalton Transactions* **2024**, *53*, 18585–18591.
[17] K. Choroba, J. Palion-Gazda, M. Penkala, P. Rawicka, B. Machura, *Dalton Trans.* **2024**, *53*, 17934–17947.
[18] S. Jing, X. Wu, D. Niu, J. Wang, C. H. Leung, W. Wang, *Molecules* **2024**, *29*, 256.
[19] P. Barretta, G. Mazzone, *Inorg. Chem. Frontiers* **2023**, *10*, 3686–3698.
[20] A. Mondal, S. Shanavas, U. Sen, U. Das, N. Roy, B. Bose, P. Paira, *RSC Adv.* **2022**, *12*, 11953–11966.
[21] A. R. Smith, P. L. Burn, B. J. Powell, *ChemPhysChem* **2011**, *12*, 2429–2438.
[22] S. K. Seth, P. Purkayastha, *Eur. J. Inorg. Chem.* **2020**, *2020*, 2990–2997.
[23] A. K. Yadav, A. Upadhyay, A. Bera, R. Kushwaha, A.-A. Mandal, S. Acharjee, A. Kunwar, S. Banerjee, *Inorg. Chem. Front.* **2024**, *11*, 5435–5448.
[24] C. Reghukumar, S. Shamjith, V. P. Murali, P. K. Ramya, K.-V. Radhakrishnan, K.-K. Maiti, *J Photochem. Photobiology B: Biology* **2024**, *250*, 112832.
[25] M. Martínez–Alonso, C. G. Jones, J. D. Shipp, D. Chekulaev, H. E. Bryant, J. A. Weinstein, *J. Bio. Inorg. Chem.* **2024**, *29*, 113–125.
[26] N. Roy, T. Dasgupta, S. Ghosh, M. Jayaprakash, M. Pal, S. Shanavas, S. Kanta Pal, V. Muthukumar, A. Senthil Kumar, R. Tamizhselvi, M. Roy, B. Bose, D. Panda, R. Chakrabarty, P. Paira, *Langmuir* **2024**, *40*, 25390–25404.
[27] N. Wu, T. Liu, M. Tian, C. Liu, S. Ma, H. Cao, H. Bian, L. Wang, Y. Feng, J. Qi, *Molecular Medicine Reports* **2023**, *29*, 24.
[28] A. Merlino, *Coord. Chem. Rev.* **2023**, *480*, 215026.
[29] B. Kar, P. Paira, *Chemistry–A Euro. J.* **2024**, 202401720.
[30] R. Kushwaha, A. Upadhyay, S. Peters, A. K. Yadav, A. Mishra, A. Bera, T. Sadhukhan, S. Banerjee, *Langmuir* **2024**, *40*, 12226–12238.
[31] R. Bresolí-Obach, M. Frattini, S. Abbruzzetti, C. Viappiani, M. Agut, S. Nonell, *Sensors* **2020**, *20*, 5952.
[32] R. Nimal, A. Shah, M. Saddiq, *J. Photochem. Photobiol.* **2020**, *2*, 100006.
[33] H. Gökce, N. Öztürk, Ü. Ceylan, Y. B. Alpaslan, G. Alpaslan, *Spectrochimica Acta Part A: Mol. Biomol. Spect.* **2016**, *163*, 170–180.

Manuscript received: November 22, 2024
Revised manuscript received: February 2, 2025
Version of record online: February 18, 2025